Article
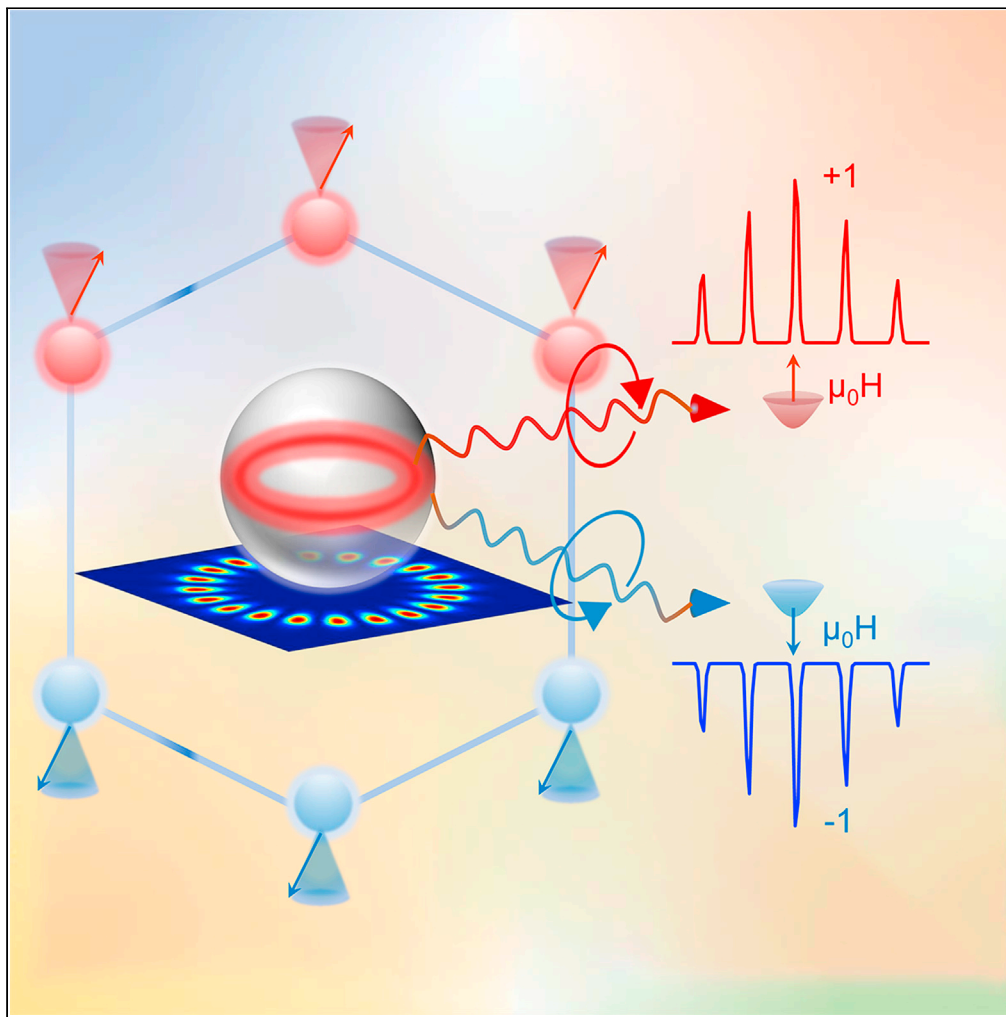
Multiwavelength magnetic coding of helical luminescence in ferromagnetic 2D layered CrI$_3$

Bo Peng, Zhiyong Chen, Yue Li, Zhen Liu, Difei Liang, Longjiang Deng

bo_peng@uestc.edu.cn (B.P.)
dfliang@uestc.edu.cn (D.L.)

Highlights

Realizing strong coupling of WGM helical emission and FM orders by SiO$_2$ cavity

Achieving reversible multiwavelength magnetic coding in the near-infrared region

Article

Multiwavelength magnetic coding of helical luminescence in ferromagnetic 2D layered CrI$_3$

Bo Peng,[1,2,3,*] Zhiyong Chen,[1,2] Yue Li,[1,2] Zhen Liu,[1,2] Difei Liang,[1,2,*] and Longjiang Deng[1,2]

SUMMARY

Two-dimensional (2D) van der Waals (vdW) ferromagnets have opened new avenues for manipulating spin at the limits of single or few atomic layers, and for creating unique magneto-exciton devices through the coupling of ferromagnetic (FM) orders and excitons. However, 2D vdW ferromagnets explored so far have rarely possessed exciton behaviors; to date, FM CrI$_3$ have been revealed to show ligand-field photoluminescence correlated with FM ordering, but typically with a broad emission peak. Here, we report a straightforward approach to realize strong coupling of narrow helical emission and FM orders in CrI$_3$ through microsphere cavity. The resonant whispering-gallery modes (WGM) of SiO$_2$ microspheres cause strong oscillation helical emissions with a full width at half-maximum (FWHM) of ∼5 nm under continuous wave excitation. Reversible magnetic coding of helical luminescence is realized in the range of 950–1100 nm. This work enables numerous opportunities for creating magnetic encoding lasing for photonic integrated chips.

INTRODUCTION

The emergence of long-range ferromagnetic orders in two-dimensional (2D) van der Waals (vdW) ferromagnetic (FM) material has provided a new avenue for creating on-chip lasers, isolators, and modulators for silicon photonics toward information processing and transmission through magneto-exciton coupling (Deng et al., 2018; Gong et al., 2017; Huang et al., 2017; Liu et al., 2020, 2021; Mak et al., 2019; Song et al., 2018; Sun et al., 2019). The magnetic orders can be switched between FM and atomic force microscope (AFM) states by magnetic field (Klein et al., 2018; Zhong et al., 2017), electric gating (Huang et al., 2018; Jiang et al., 2018a, 2018b; Zhang et al., 2020), electrostatic doping (Jiang et al., 2018a; Zheng et al., 2020), and hydrostatic pressure (Li et al., 2019; Song et al., 2019), which empower a pivotal foundation for realizing magnetic and electric control of magneto-optical coupling for information transfer. 2D vdW bilayer CrI$_3$ FM insulators used as spin valve in a magnetic tunneling junction device have highlighted flexibilities for encoding information and data storage (Jiang et al., 2018a; Klein et al., 2018; Song et al., 2018). To date, diverse 2D vdW FM and AFM metal, insulators, and even semiconductors have been explored (Liu et al., 2021). FM Cr$_2$Ge$_2$Te$_6$ few-layer have demonstrated a p-type semiconducting behavior and gate-controllable magnetism (Jiang et al., 2018a; Verzhbitskiy et al., 2020); few-layer Fe$_3$GeTe$_2$ FM metal have shown high Curie temperature (Tc) above room temperature through ionic/protonic gating, patterning, and interfacial exchange coupling (Deng et al., 2018; Li et al., 2018; May et al., 2019; Wang et al., 2020a); magnetic topological insulator MnBi$_2$Te$_4$ has recently been reported to present layer-dependent magnetic phase and spin-flop behaviors (Deng et al., 2020; Yang et al., 2021). Alternatively, air-stable metallic 2D vdW CrTe$_2$ and CrSe$_2$ with thickness-dependent magnetic orders have been directly synthesized by chemical vapor deposition (CVD) methods (Li et al., 2021; Meng et al., 2021). However, thus far, few 2D vdW magnets have been revealed luminescence and exciton behaviors, and none examining magnetic coding of photoluminescence (PL), despite the discovery of luminescence in FM CrI$_3$ and AFM NiPS$_3$ (Hwangbo et al., 2021; Kang et al., 2020; Seyler et al., 2017; Wang et al., 2021). Moreover, the PL of CrI$_3$ derives from a ligand-field-allowed d-d transition, which naturally leads to a very broad PL peak with an FWHM of 100–200 nm owing to strong vibronic coupling (Seyler et al., 2017), extremely limiting the potential for photonic devices; in addition, it is difficult to achieve magnetic/electric control of spin in AFM NiPS$_3$, due to a high critical field up to 10 T at least (Wang et al., 2021).

With the rapid development of digitalization and semiconductor optoelectronics technology, various fields have an increasing demand for on-chip lasers, so the research on high-performance and miniaturized

[1]National Engineering Research Center of Electromagnetic Radiation Control Materials, School of Electronic Science and Engineering, University of Electronic Science and Technology of China, Chengdu 611731, China

[2]State Key Laboratory of Electronic Thin Films and Integrated Devices, University of Electronic Science and Technology of China, Chengdu 611731, China

[3]Lead contact

*Correspondence:
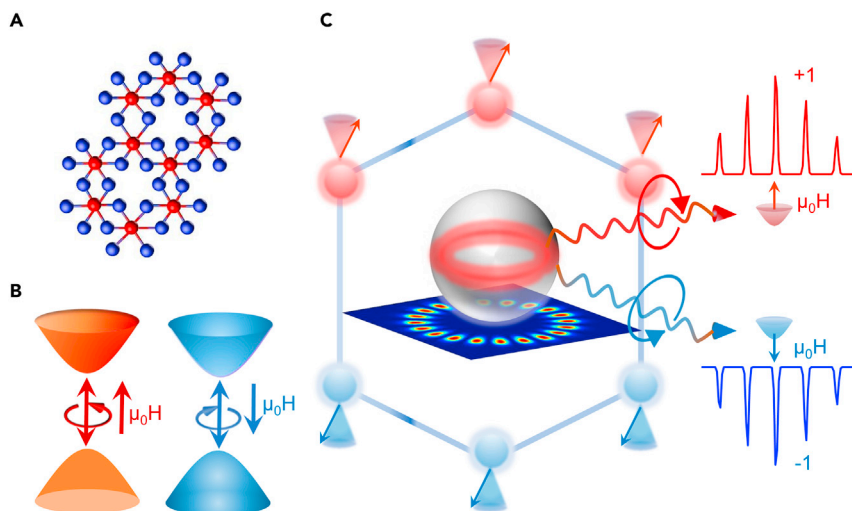bo_peng@uestc.edu.cn
(B.P.),
dfliang@uestc.edu.cn (D.L.)
https://doi.org/10.1016/j.isci.2021.103623

Figure 1. CrI$_3$/microsphere WGM microcavities

(A) Atomic structure of monolayer CrI$_3$. Red and blue balls represent Cr and I atoms, respectively.

(B) Schematic of magnetic control of right-hand (red) and left-hand (blue) circularly polarized PL light.

(C) Magnetic encoding of WGM PL in CrI$_3$/microsphere cavities. Strong WGM oscillations lead to narrow circularly polarized WGM PL associated with magnetic orders upon excitation by circular polarization-resolved light.

on-chip lasers is of great significance (Gao et al., 2020; Kyeremateng et al., 2017). On-chip lasers have broad application prospects, such as a light source for on-chip integrated photonic chips, laser scanning, and ranging or flexible displays. Traditional directly modulated lasers (DML) have been achieved by injecting the pump current to the gain medium, and the modulation speed is affected by its volume of the active region and relaxation oscillation frequency (Dong et al., 2018; Kobayashi et al., 2013). Alternatively, topological lasers with single-mode lasing and robustness against defects have been realized by coupling of photonic gain with topological structure (Bandres et al., 2018). Additionally, atomic-thin lasers using transition metal dichalcogenides (TMDs) with strong exciton emission as optical gain medium have been recently reported (Li et al., 2017; Salehzadeh et al., 2015; Wu et al., 2015; Ye et al., 2015). However, thus far, small-volume atomic-thin lasers with intrinsic magnetism in the near-infrared (NIR) region have been still elusive, which provide numerous opportunities to realized magnetic-field controlled DML. Moreover, the NIR laser is more challenging owing to the lack of gain medium with strong NIR emission.

Here, we report the realization of magnetic control and coding of NIR whispering-gallery-mode (WGM) emission through coupling of the luminescence of 2D ferromagnetic CrI$_3$ and SiO$_2$ microsphere cavities. Circularly polarized WGM PL features in CrI$_3$/microsphere are coupled with CrI$_3$ magnetic orders. The right-handed (left-handed) polarized WGM PL is dominated in a positive (negative) magnetic field of +1 T (−1 T). Multiwavelength encoding is realized through repeatedly manipulating helicity of each WGM PL peak by magnetic field. This work opens the door to creating new atomically thin 2D magneto-optical devices for photonic integrated circuit and on-chip optical system.

RESULTS AND DISCUSSION

Coupling of magnetic orders and PL in CrI$_3$

In 2D FM CrI$_3$ monolayer, Cr^{3+} ions in each layer are coordinated by six nonmagnetic I$^-$ ions to form an octahedron (Guo et al., 2020), which shares edges to build a honeycomb network (Figure 1A). Monolayer CrI$_3$ is a Ising ferromagnetism arising from the Cr-I-Cr superexchange interaction, which is described by the Ising spin Hamiltonian, $H = -(1/2)\sum(J_{xy} S_{i(x)}S_{j(x)} + J_{xy} S_{i(y)}S_{j(y)} + J_z S_{i(z)}S_{j(z)})$, where $S_{i(x, y, z)}$ and $S_{j(x, y, z)}$ are the spin along the x, y, z direction of Cr^{3+} at $i(j)$ sites; J_{xy} and J_z are the exchange coupling term of in-plane and out-of-plane spin components and $J_z > J_{xy} > 0$ in Ising FM model. In few-layer CrI$_3$, intra-atomic d-d transitions and charge-transfer transitions owing to ligand field lead to a broad layer-dependent PL emission at ~1020 nm with an FWHM of ~100 nm (Figure S1) (Seyler et al., 2017). PL intensities show strong layer dependence and significantly increase as increasing layers (Seyler et al., 2017); therefore, thick CrI$_3$ flakes
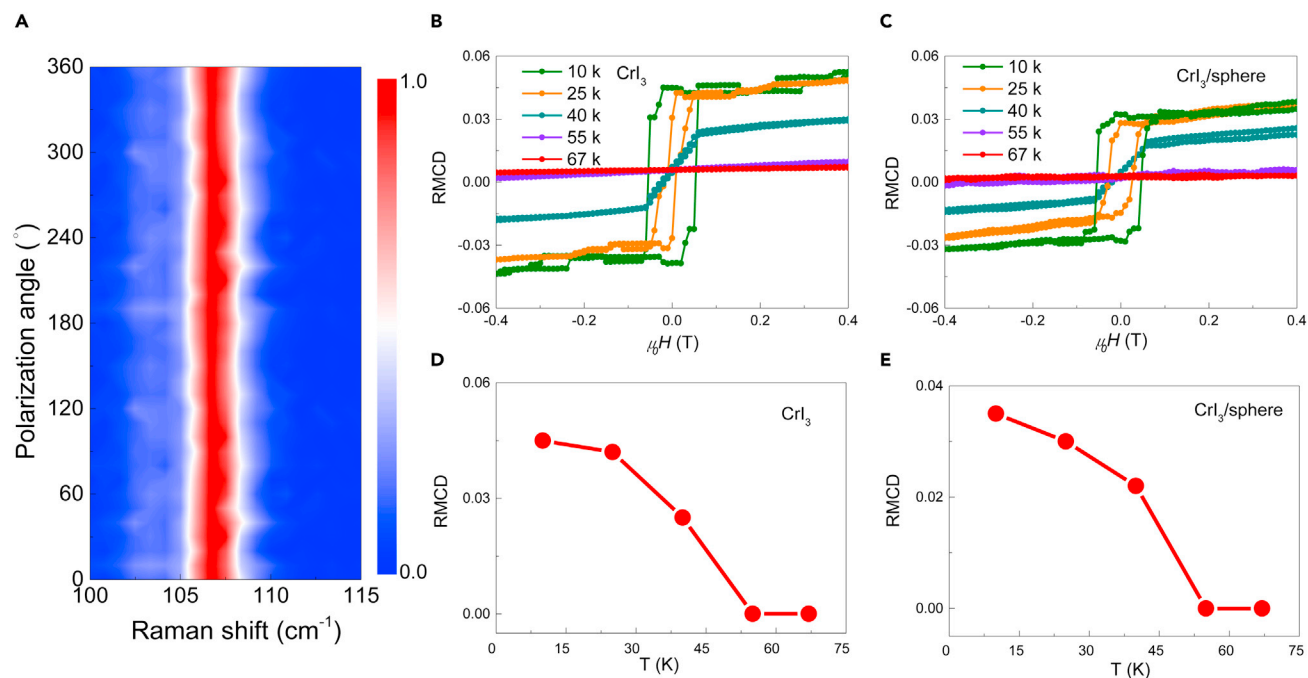
Figure 2. Polarization-dependent Raman and RMCD measurements of CrI₃/microsphere and bare CrI₃

(A) Polarization-angle dependent Raman maps of the CrI_3 bulk beneath a 10 μm SiO_2 microsphere.

(B and C)Temperature-dependent RMCD measurements of the bare CrI_3 and CrI_3/microsphere (10 μm).

(D and E) Extracted RMCD intensities as a function of temperature from (B and C), showing a Tc of ~50 K.

and bulk were chosen in our experiments. The helicity of the absorption and associated PL emission is correlated with the spin of the electrons at the ground states. Spin states are tied to magnetic orders of CrI_3 few-layers. Thus, in an out-of-plane positive magnetic field, the upper spin states are dominated and absorb right-hand polarized light, consequentially mostly giving right-hand polarized PL emission (Figure 1B); when the magnetic field turns downward, the spins of electrons are reversed, and mainly lead to left-hand polarized PL (Figure S1). But, the poor and broad PL features restrict the exploring on magneto-exciton coupling and creating photonic devices with unique functions. Optical microcavities have been widely applied to enhance light-matter interaction and suppress FWHM for realizing strong emission and lasing (Salehzadeh et al., 2015; Schwarz et al., 2014; Wu et al., 2014; Ye et al., 2015). SiO_2 microsphere as high-quality WGM microcavities with high Q-factor of ~10^8 can significantly enhance the coupling between gain medium and optical cavity modes (Mi et al., 2017; Zhao et al., 2018). Thus, SiO_2 microsphere cavities can be coupled with FM 2D layered CrI_3 to create narrow and strong WGM oscillation PL peaks. The coupling between circularly polarized PL emission and SiO_2 spherical microcavities obey the law of conservation of angular momentum; thus, the PL helicity associated with magnetic orders are preserved. In a positive magnetic field, right-hand polarization-resolved WGM oscillation PL originating from spin-up states are dominated, and vice versa (Figure 1C). Polarization-resolved Raman spectra show that thick layered CrI_3 bulk sample adopts a rhombohedral structure at 10 K. Raman shift of the two-fold degenerated E_g mode at ~107 cm^{-1} are independent of the polarization angle (Figures 2A and S2), validating the high-symmetry rhombohedral phase (Li et al., 2019; Song et al., 2019). Reflective magnetic circular dichroism (RMCD) was used to probe the long-range FM orders. A 633 nm continuous-wave laser was applied as an excitation source with the light spot size of ~2 μm and 2 μW. Figures 2B and 2C show the typical RMCD curve of bare CrI_3 and CrI_3 beneath SiO_2 sphere. Striking hysteresis loops are observed on both bare CrI_3 and CrI_3 beneath SiO_2 sphere below 55 K, indicating a Tc of ~50 K, and the SiO_2 microsphere cavities do not influence the Tc of CrI_3.

Magnetic control of WGMPL emission of CrI₃

To obtain strong enhancements, SiO_2 microspheres with 10 and 12.5 μm diameter were transferred onto mechanically exfoliated thick CrI_3 flakes (~32 nm) and bulk (~55 nm) through polydimethylsiloxane

(PDMS) films (Figure S2). The Q factors of SiO_2 spherical cavities were firstly estimated on MoS_2/SiO_2 samples. The Q factors of microsphere cavities are estimated from $Q = \lambda/\delta\lambda$, where $\delta\lambda$ is the FWHM of the WGMs, and the Q factor for the $TM_{1,61}$ mode ($\sim$633 nm) can reach about 1055(Figure S3). As shown in Figure S3B, the PL intensity increases sharply with increasing excitation light power, and the lasing behavior at the $TM_{1,61}$ mode ($\sim$633 nm) is observed. Figure S3C shows PL intensity of MoS_2/SiO_2 and MoS_2 as a function of laser power. The PL intensities of MoS_2 shows a linear dependence on the excitation light power, and $TM_{1,61}$ mode shows a kink indicating the onset of superlinear emission. In Figure S3D, the FWHM of $TM_{1,61}$ mode decreases from 0.9 to 0.6 nm, the linewidth narrowing effect further confirms the appearance of lasing. Room temperature lasing from MoS_2/sphere validates that Q-factor of SiO_{-2} is high enough for WGM lasing (Zhao et al., 2018). WGM PL peaks in the range of $\sim$900–1100 nm are unambiguously observed from CrI_3 beneath 10 and 12.5 μm SiO_2 spheres under continuous wave 633 nm excitation with 1 mW (Figure S4 and related to STAR Methods). SiO_2 microsphere optical cavities enhance PL intensity of CrI_3 by $\sim$2.7 times as compared with that from the same but bare CrI_3. The excitation area can be effectively reduced to enhance the coupling between the gain region and the optical mode due to the lens effect of the microspheres (Mi et al., 2017; Zhao et al., 2018), which increases the spontaneous emission efficiency and PL intensity of CrI_3. In stark contrast, no oscillation peak is detected in bare CrI_3 sample. Theoretical calculations demonstrate that the strong WGM PL is attributed to the first-order TM modes (TM_1), as indicated by blue line (Figure S4).

To study the WGM PL in the microsphere cavity, power-dependent PL spectra were recorded on CrI_3/microsphere vertical light-emitting gain structure in the range from 10 μW to 1.5 mW with a 633 nm laser excitation source at 10 K. The lensing and screening effects of the microsphere cavity increase the excitation efficiency of CrI_3, the equally spaced oscillation peaks can be distinguished, even the excitation power is as low as about 10 μW (Figures S5 and S6). The WGM PL intensities linearly increase with laser power increasing. When the laser power is increased to 1.5 mW, the oscillation peak intensity increases sharply and the peak width is narrowed. The spacing between two adjacent resonant modes remains constant with increasing laser power, indicating the WGM PL originating from the same resonant modes of the sphere cavities. The PL intensities of bare CrI_3 samples also linearly increase with the increase of laser power, but smaller than WGM PL intensity. The integrated PL intensities of $TM_{1,36}$, $TM_{1,37}$, $TM_{1,47}$, and $TM_{1,48}$ modes of CrI_3/microsphere with 10 and 12.5 μm SiO_2 spheres remain linear to the excitation power density. With further increasing laser power, the WGM oscillation peak intensity of the sample achieves maximum at 2.6 mW and drastically decrease at 3.0 mW due to laser burning of CrI_3 flakes. But, no transition from spontaneous emission to amplified spontaneous emission was observed (Figures S5 and S6). This may be because the gain of CrI_3 flakes is not strong enough and they are also easy to burn out under high power, resulting in no superlinear response. The PL intensity of thin CrI_3 was strongly dependent on the number of layers, and decrease with decreasing thickness of CrI_3. Even, no WGM peaks are observed and only PL enhancement behaviors take place if the gain of CrI_3 is decreased by applying thin CrI_3 flakes (Figure S7). WGM PL features are nearly same in 10 and 12.5 μm SiO_2 microsphere cavities. Therefore, we focus on 10 μm SiO_2 microcavities to further study the magnetic control and coding of WGM PL.

WGM PL of CrI_3/microsphere can be manipulated by an out-of-plane magnetic field. Figure 3 presents the circularly polarization-resolved WGM PL features from CrI_3/microsphere at 10 K, at magnetic field +1, 0, −1, and 0 T, respectively. We define the right-hand (left-hand) circularly polarized PL spectra upon excitation by right-hand (left-hand) circularly polarized laser as RR (LL). The intensity of circularly polarized WGM PL is correlated to magnetic orders of CrI_3. In a magnetic field of +1 T, the FM orders are spin-up, leading to that the spin-up states are dominated; therefore, RR WGM PL is stronger than LL WGM PL (Figures 3A and 3E). As the magnetic field is lowered to 0 T, the CrI_3 shows an antiferromagnetic behavior, and spin-up and spin-down states are nearly equal (Figures 3B and 3E). When magnetic field is further reversed to −1 T, spin states are also inversed, giving rise to opposite helicity and exhibiting a stronger LL component than RR (Figures 3C and 3E). When magnetic field returns back to 0 and +1 T, the WGM PL is also recovered (Figures 3D and 3A). The corresponding RMCD results clearly show the associated FM and AFM orders, which consist with the magnetic control behaviors of circularly polarization-resolved WGM PL. It should be noted that the intensity variations of right-handed and left-handed polarized PL of the CrI_3/sphere are lower than the same pure CrI_3 flakes (Figure 3 and Figure S1). This probably results from the decrease of magnetic anisotropy and long-range ferromagnetic orders induced by tensile strains, which are formed during the transferring SiO_2 sphere onto CrI_3 by a PPMA fixed-point transfer method.
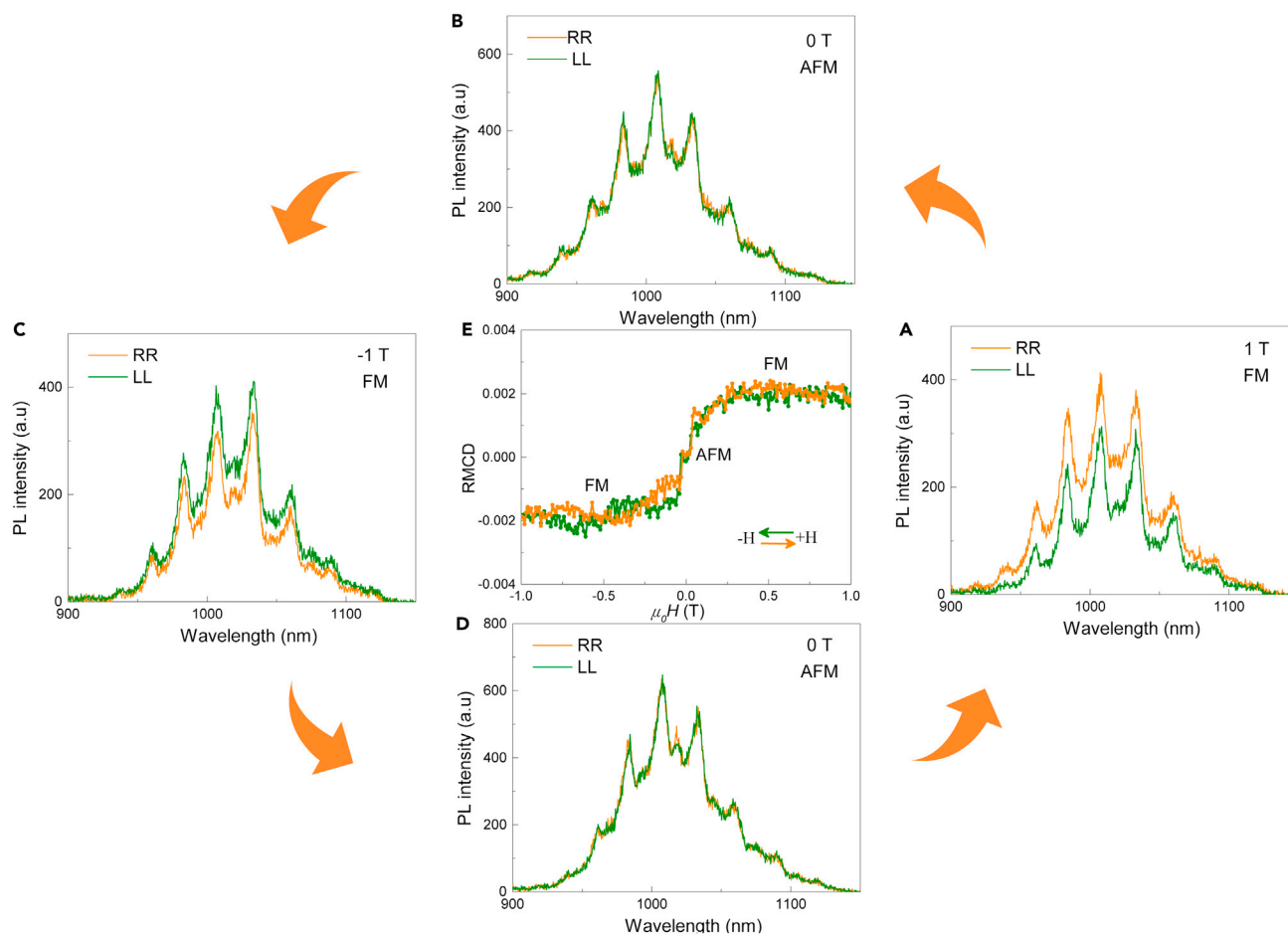
Figure 3. Magnetic control of WGM PL of CrI$_3$ beneath a 10 μm SiO$_2$ microsphere

(A–D) Circularly polarized PL spectra upon 2 mW 633 nm excitation with magnetic field at +1, 0,−1, and 0 T.

(E) Corresponding RMCD curve as a function of magnetic field, which is consistent with the magnetic control of WGM PL.

Previous reports have demonstrated that tensile strains lead to an increase of bandgap associated with unchanged valence band maximum (VBM) and higher conduction band minimum (CBM) (Webster and Yan, 2018; Zhang et al., 2015). FigureS7B shows that the PL peak is blue-shifted to a high energy, which indicates that tensile strains are formed on CrI$_3$ flakes. Tensile strains lead to the increase of the Cr-I-Cr angle and bond length, which result in decreasing magnetic anisotropy energies and ferromagnetic orders of CrI$_3$. The helicity of PL emission of CrI$_3$ is strongly tied to magnetic orders. Therefore, the intensity variations of circularly polarized PL of CrI$_3$/sphere decrease.

Multiwavelength magnetic encoding

The WGM oscillation modes of sphere cavities result in a series of narrow PL at multiwavelength. We studied the multiwavelength magnetic encoding of circularly polarized PL through recycling a loop of magnetic field between +1 and −1 T. Magnetic field loop is set from +1 to 0 T and inversely increase to −1 T, and return back to +1 T (Figure 4A). The PL intensity differences between LL and RR WGM PL, defined as ΔI, show striking narrow oscillation peaks at 976, 995, 1020, 1045, and 1070 nm with FWHM between 5 and 10 nm (Figure 4B), which show an obvious magnetic-field dependent behavior. ΔI at the five distinct wavelengths are opposite at +1 and −1 T, and much larger than that at 0 T, which provide a rich platform for tri-state encoding through on/off switching of magnetic field. Figure 4B shows ten recycling of ΔI for multiwavelength magnetic encoding. The ΔI features at 1020 ± 5, 1070 ± 5, 1045 ± 5, and 995 ± 5 nm were extracted. Each wavelength presents +1, 0, and −1 tri-states at magnetic field of +1, 0, and -1T. The magnetic control behaviors of tri-states are entirely correlated to the magnetic field and display the
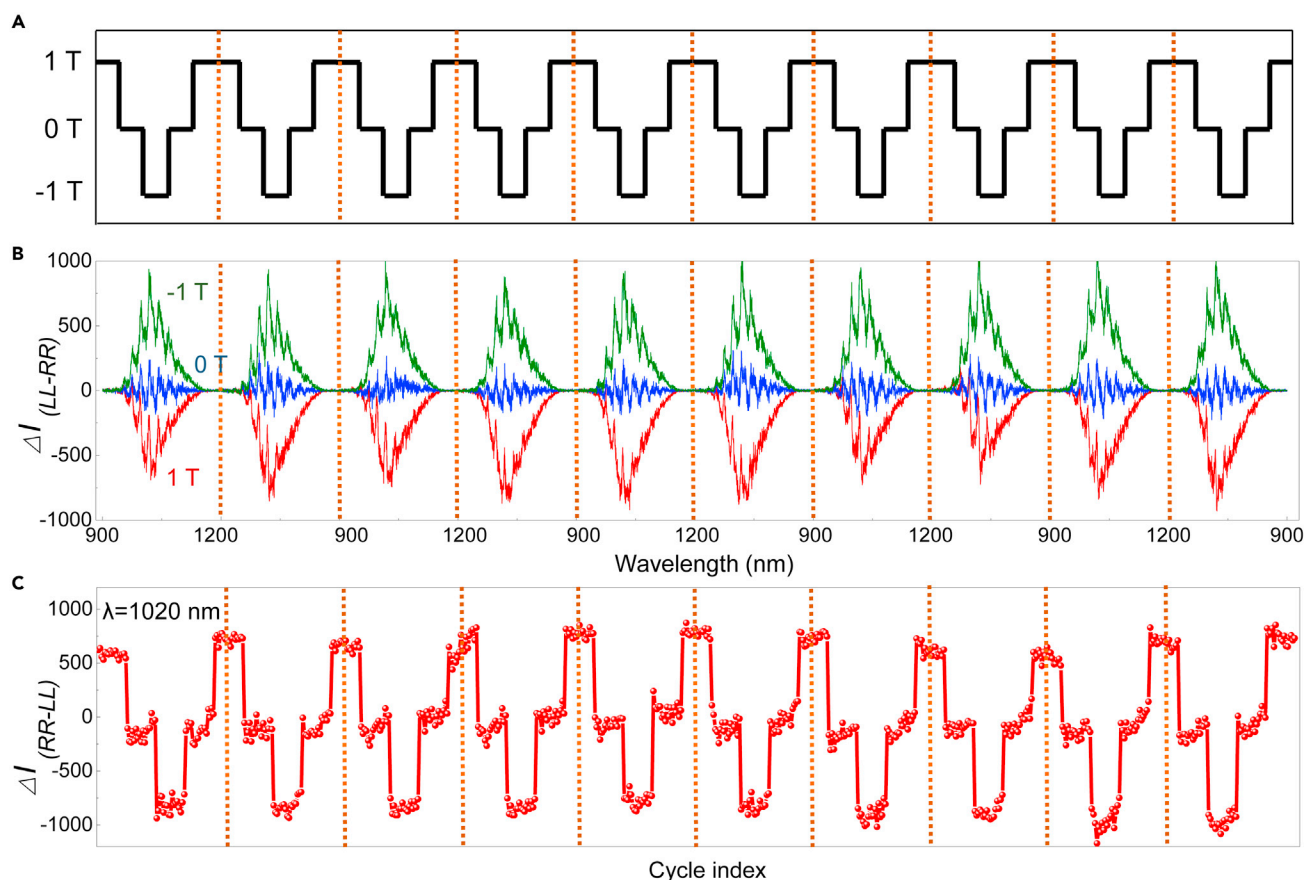
Figure 4. Reversible magnetic control and coding of helical luminescence in the CrI₃/microsphere

(A) Schematic of the cycle-dependent magnetic field setup with a sequence of 1 T, 0 T,−1 T, 0 T, and 1 T.

(B) Recycling control of PL intensity difference between helical WGM PL of CrI₃/microsphere upon 2 mW 633 nm excitation by magnetic field.

(C) Magnetic control and tri-state coding of WGM PL peaks at 1020 nm extracted from Figure 4B.

same shape with magnetic field setups, as shown in Figures 4C and 5. The helicity of CrI₃/microsphere WGM oscillation peaks are determined by magnetic orders of CrI₃ and controlled by magnetic field, which also can be used to achieve magnetic encoding function. Similar magnetic-field control behaviors have been achieved on different samples (Figures 4B and 3), although the PL intensity variations is different, which strongly validate that the SiO₂ spherical cavities can generally lead to WGM peaks for CrI₃ ferromagnetism and reversible magnetic control and coding of helical luminescence in the CrI₃/microsphere is reproducible. The degree of polarization (DOP) from CrI₃/microsphere and CrI₃ is given by DOP = (I_{RR}–I_{LL})/(I_{LL} + I_{RR}), where I_{RR} and I_{LL} are the intensity of right-hand and left-hand circularly polarized PL (Li et al., 2020; Peng et al., 2017; Wang et al., 2020b). When a magnetic field of +1 T is applied, DOP of the WGM PL is around +10%, while the DOP is inversely changed to −10% in a −1 T magnetic field, owing to the reversal of the magnetization of CrI₃ (Figure 6). Magnetic fields manipulate the DOP of each oscillation peak in ten recycling, clearly validating multiwavelength magnetic encoding behaviors.

Conclusions

In summary, we demonstrated magnetic control of NIR helical WGM PL and realized tri-state encoding at different wavelength. The lensing and screening effects of SiO₂ microspheres increase the spontaneous emission efficiency of CrI₃ to create unambiguous WGM oscillation peaks which is coupled with magnetic orders of CrI₃. Magnetic fields manipulate and control each WGM peak, and the PL helicity and intensity difference of every WGM peak are applied to realize multiwavelength encoding through recycling magnetic fields. This work provides promising opportunities for creating magneto-optical
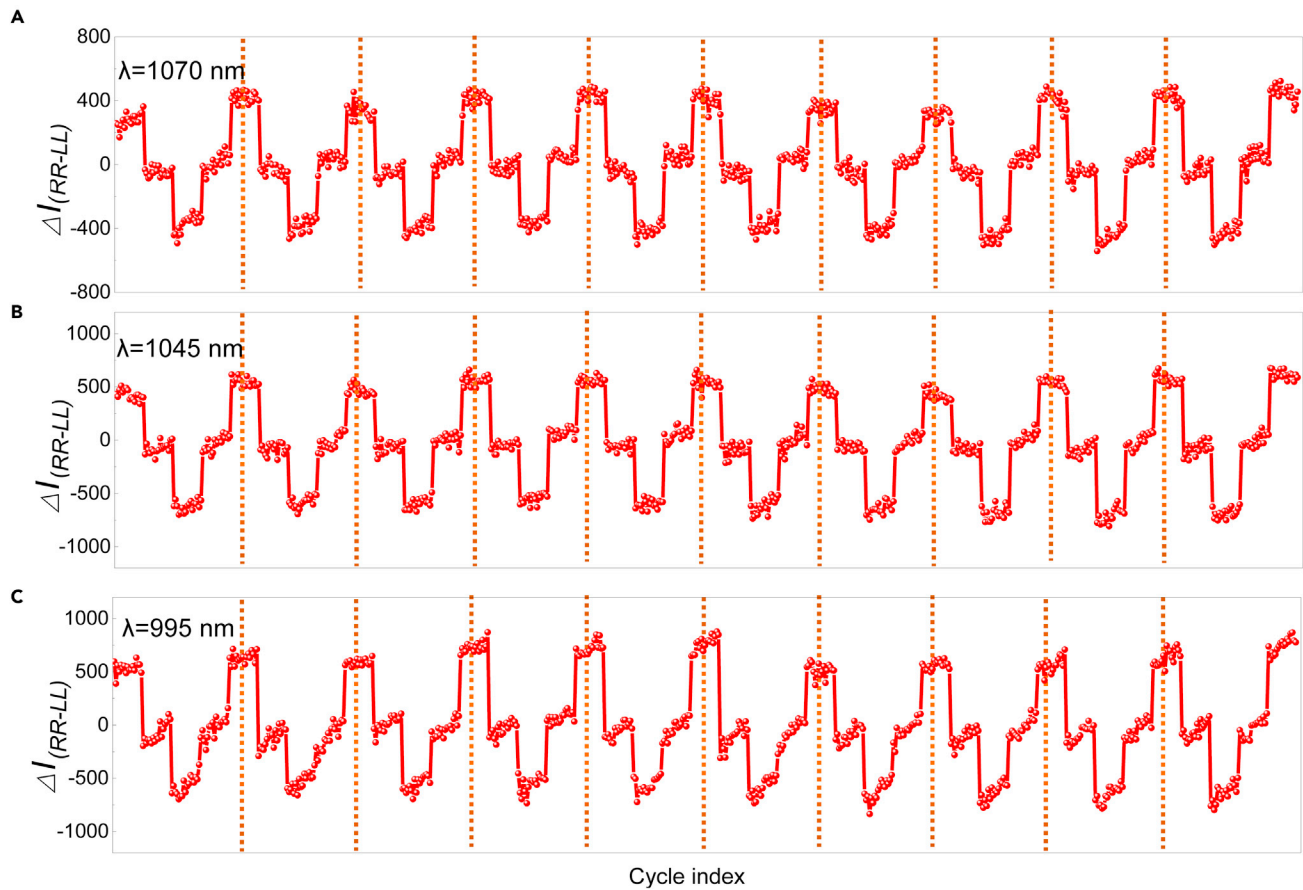
Figure 5. Multiwavelength magnetic coding through PL intensity difference of helical WGM luminescence
(A–C) Reversible magnetic control and tri-state coding at 1070, 1045, and 995 nm in selected magnetic fields of +1, 0, and −1 T, respectively.

devices and integrated photonic lasing with magnetic encoding function through FM 2D materials microcavity.

Limitations of the study

The CrI_3 sample needs to be mechanically exfoliated in a glove box, and the sample should not be exposed to the air, otherwise the sample will be hydrolyzed.

STAR★METHODS

Detailed methods are provided in the online version of this paper and include the following:

- KEY RESOURCES TABLE
- RESOURCE AVAILABILITY
  - Lead contact
  - Materials availability
  - Date and code availability
- EXPERIMENTAL MODEL AND SUBJECT DETAILS
  - Sample preparation
  - Optical measurements
- METHOD DETAILS
  - Materials
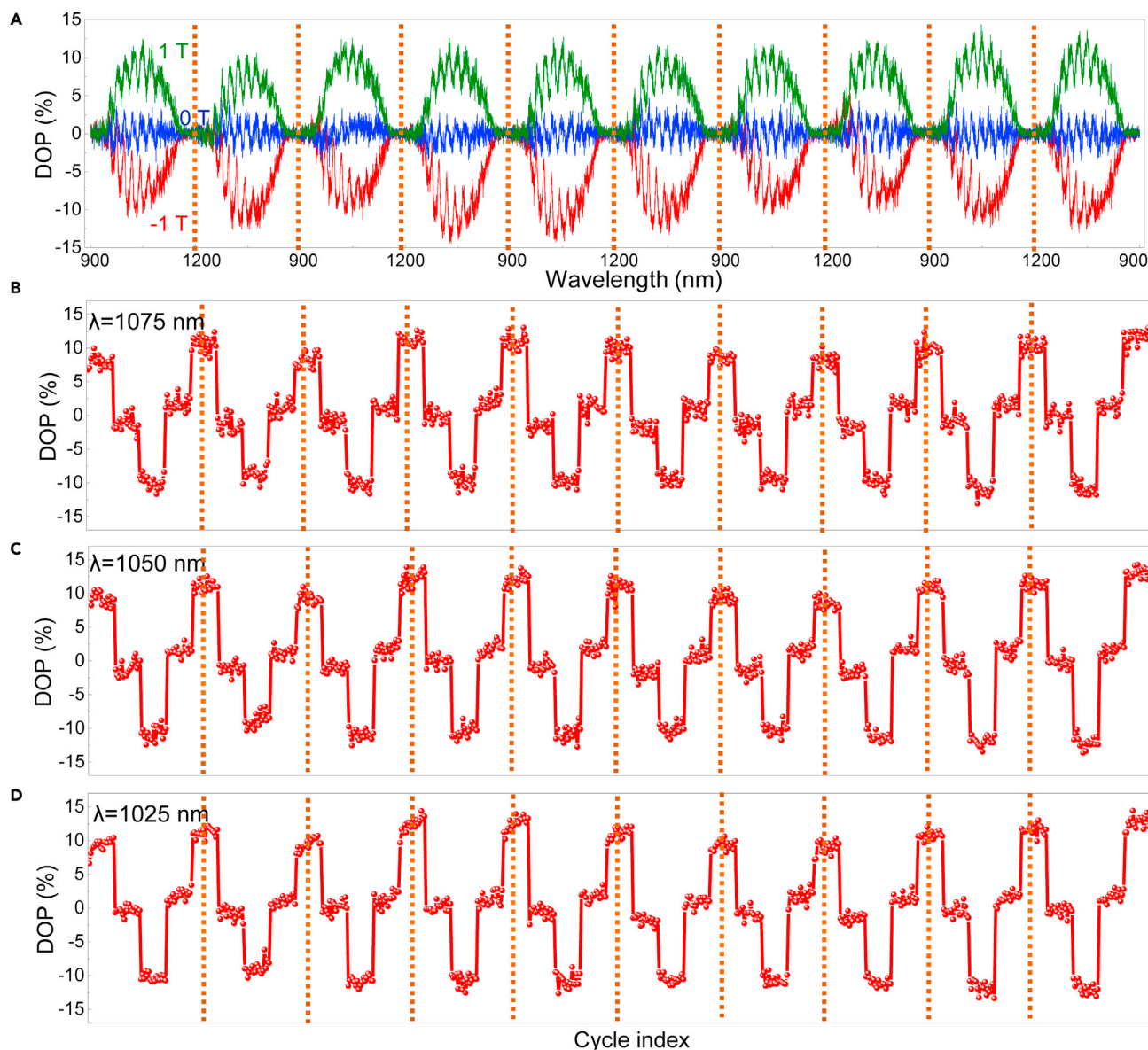 - CrI_3 synthesis
  - Sample preparation

Figure 6. Multiwavelength magnetic coding through helicity of WGM luminescence

(A) Recycling magnetic control of DOP.

(B–D) Corresponding tri-state magnetic encoding of DOP at 1075, 1050, and 1025 nm in selected magnetic fields of +1, 0, and −1 T, respectively.

- QUANTIFICATION AND STATISTICAL ANALYSIS
  - Scanning electron microscopy (SEM)
  - Raman spectroscopy
  - Photoluminescence spectroscopy
  - Reflective magnetic circular dichroism spectroscopy

SUPPLEMENTAL INFORMATION

Supplemental information can be found online at https://doi.org/10.1016/j.isci.2021.103623.

ACKNOWLEDGMENTS

AUTHOR CONTRIBUTIONS

B.P. developed the concept and designed the experiment. B.P., Z.Y.C, L.J.D, and D.F.L prepared the manuscript and discussed the mechanism of magnetic encoding. Z.Y.C and Z.L. prepared the samples and performed the PL and Raman measurements. Y.L. contributed to fully relativistic calculations.

DECLARATION OF INTERESTS

The authors declare no competing interests.

REFERENCES

Bandres, M.A., Wittek, S., Harari, G., Parto, M., Ren, J., Segev, M., Christodoulides, D.N., and Khajavikhan, M. (2018). Topological insulator laser: Experiments. Science 359. https://doi.org/10.1126/science.aar4005.

Deng, Y., Yu, Y., Shi, M.Z., Guo, Z., Xu, Z., Wang, J., Chen, X.H., and Zhang, Y. (2020). Quantum anomalous Hall effect in intrinsic magnetic topological insulator MnBi$_2$Te$_4$. Science 367, 895–900. https://doi.org/10.1126/science.aax8156.

Deng, Y., Yu, Y., Song, Y., Zhang, J., Wang, N.Z., Sun, Z., Yi, Y., Wu, Y.Z., Wu, S., Zhu, J., et al. (2018). Gate-tunable room-temperature ferromagnetism in two-dimensional Fe$_3$GeTe$_2$. Nature 563, 94–99. https://doi.org/10.1038/s41586-018-0626-9.

Dong, P., Maho, A., Brenot, R., Chen, Y.-K., and Melikyan, A. (2018). Directly reflectivity modulated laser. J. Light. Technol. 36, 1255–1261. https://doi.org/10.1109/jlt.2018.2791363.

Gao, Y., Lo, J.-C., Lee, S., Patel, R., Zhu, L., Nee, J., Tsou, D., Carney, R., and Sun, J. (2020). High-power, narrow-linewidth, miniaturized silicon photonic tunable laser with accurate frequency control. J. Light. Technol. 38, 265–271. https://doi.org/10.1109/jlt.2019.2940589.

Gong, C., Li, L., Li, Z., Ji, H., Stern, A., Xia, Y., Cao, T., Bao, W., Wang, C., Wang, Y., et al. (2017). Discovery of intrinsic ferromagnetism in two-dimensional van der Waals crystals. Nature 546, 265–269. https://doi.org/10.1038/nature22060.

Guo, K., Deng, B., Liu, Z., Gao, C., Shi, Z., Bi, L., Zhang, L., Lu, H., Zhou, P., Zhang, L., et al. (2020). Layer dependence of stacking order in nonencapsulated few-layer CrI$_3$. Sci. China Mater. 63, 413–420. https://doi.org/10.1007/s40843-019-1214-y.

Huang, B., Clark, G., Klein, D.R., MacNeill, D., Navarro-Moratalla, E., Seyler, K.L., Wilson, N., McGuire, M.A., Cobden, D.H., Xiao, D., et al. (2018). Electrical control of 2D magnetism in bilayer CrI$_3$. Nat. Nanotechnol. 13, 544–548. https://doi.org/10.1038/s41565-018-0121-3.

Huang, B., Clark, G., Navarro-Moratalla, E., Klein, D.R., Cheng, R., Seyler, K.L., Zhong, D., Schmidgall, E., McGuire, M.A., Cobden, D.H., et al. (2017). Layer-dependent ferromagnetism in a van der Waals crystal down to the monolayer limit. Nature 546, 270–273. https://doi.org/10.1038/nature22391.

Hwangbo, K., Zhang, Q., Jiang, Q., Wang, Y., Fonseca, J., Wang, C., Diederich, G.M., Gamelin, D.R., Xiao, D., Chu, J.-H., et al. (2021). Highly anisotropic excitons and multiple phonon bound states in a van der Waals antiferromagnetic insulator. Nat. Nanotechnol. 16, 655–660. https://doi.org/10.1038/s41565-021-00873-9.

Jiang, S., Li, L., Wang, Z., Mak, K.F., and Shan, J. (2018a). Controlling magnetism in 2D CrI$_3$ by electrostatic doping. Nat. Nanotechnol. 13, 549–553. https://doi.org/10.1038/s41565-018-0135-x.

Jiang, S., Shan, J., and Mak, K.F. (2018b). Electric-field switching of two-dimensional van der Waals magnets. Nat. Mater. 17, 406–410. https://doi.org/10.1038/s41563-018-0040-6.

Kang, S., Kim, K., Kim, B.H., Kim, J., Sim, K.I., Lee, J.-U., Lee, S., Park, K., Yun, S., Kim, T., et al. (2020). Coherent many-body exciton in van der Waals antiferromagnet NiPS$_3$. Nature 583, 785–789. https://doi.org/10.1038/s41586-020-2520-5.

Klein, D.R., MacNeill, D., Lado, J.L., Soriano, D., Navarro-Moratalla, E., Watanabe, K., Taniguchi, T., Manni, S., Canfield, P., Fernández-Rossier, J., et al. (2018). Probing magnetism in 2D van der Waals crystalline insulators via electron tunneling. Science 360, 1218–1222. https://doi.org/10.1126/science.aar3617.

Kobayashi, W., Ito, T., Yamanaka, T., Fujisawa, T., Shibata, Y., Kurosaki, T., Kohtoku, M., Tadokoro, T., and Sanjoh, H. (2013). 50-Gb/s direct modulation of a 1.3-μm InGaAlAs-based DFB laser with a ridge waveguide structure. IEEE J. Sel. Top. Quantum Electron. 19, 1500908. https://doi.org/10.1109/jstqe.2013.2238509.

Kyeremateng, N.A., Brousse, T., and Pech, D. (2017). Microsupercapacitors as miniaturized energy-storage components for on-chip electronics. Nat. Nanotechnol. 12, 7–15. https://doi.org/10.1038/nnano.2016.196.

Li, B., Wan, Z., Wang, C., Chen, P., Huang, B., Cheng, X., Qian, Q., Li, J., Zhang, Z., Sun, G., et al. (2021). Van der Waals epitaxial growth of air-stable CrSe$_2$ nanosheets with thickness-tunable magnetic order. Nat. Mater. https://doi.org/10.1038/s41563-021-00927-2.

Li, Q., Yang, M., Gong, C., Chopdekar, R.V., N'Diaye, A.T., Turner, J., Chen, G., Scholl, A., Shafer, P., Arenholz, E., et al. (2018). Patterning-induced ferromagnetism of Fe$_3$GeTe$_2$ van der Waals materials beyond room temperature. Nano Lett. 18, 5974–5980. https://doi.org/10.1021/acs.nanolett.8b02806.

Li, Q., Zhao, X., Deng, L., Shi, Z., Liu, S., Wei, Q., Zhang, L., Cheng, Y., Zhang, L., Lu, H., et al. (2020). Enhanced valley Zeeman splitting in Fe-doped monolayer MoS$_2$. ACS Nano 14, 4636–4645. https://doi.org/10.1021/acsnano.0c00291.

Li, T., Jiang, S., Sivadas, N., Wang, Z., Xu, Y., Weber, D., Goldberger, J.E., Watanabe, K., Taniguchi, T., Fennie, C.J., et al. (2019). Pressure-controlled interlayer magnetism in atomically thin CrI$_3$. Nat. Mater. 18, 1303–1308. https://doi.org/10.1038/s41563-019-0506-1.

Li, Y., Zhang, J., Huang, D., Sun, H., Fan, F., Feng, J., Wang, Z., and Ning, C.Z. (2017). Room-temperature continuous-wave lasing from monolayer molybdenum ditelluride integrated with a silicon nanobeam cavity. Nat. Nanotechnol. 12, 987–992. https://doi.org/10.1038/nnano.2017.128.

Liu, Z., Deng, L., and Peng, B. (2021). Ferromagnetic and ferroelectric two-dimensional materials for memory application. Nano Res. 14, 1802–1813. https://doi.org/10.1007/s12274-020-2860-3.

Liu, Z., Guo, K., Hu, G., Shi, Z., Li, Y., Zhang, L., Chen, H., Zhang, L., Zhou, P., Lu, H., et al. (2020). Observation of nonreciprocal magnetophonon effect in nonencapsulated few-layered CrI$_3$. Sci. Adv. 6, eabc7628. https://doi.org/10.1126/sciadv.abc7628.

Mak, K.F., Shan, J., and Ralph, D.C. (2019). Probing and controlling magnetic states in 2D layered magnetic materials. Nat. Rev. Phys. 1, 646–661. https://doi.org/10.1038/s42254-019-0110-y.

May, A.F., Ovchinnikov, D., Zheng, Q., Hermann, R., Calder, S., Huang, B., Fei, Z., Liu, Y., Xu, X., and McGuire, M.A. (2019). Ferromagnetism near room temperature in the cleavable van der Waals crystal Fe$_5$GeTe$_2$. ACS Nano 13, 4436–4442. https://doi.org/10.1021/acsnano.8b09660.

Meng, L., Zhou, Z., Xu, M., Yang, S., Si, K., Liu, L., Wang, X., Jiang, H., Li, B., Qin, P., et al. (2021).

Anomalous thickness dependence of Curie temperature in air-stable two-dimensional ferromagnetic 1T-CrTe$_2$ grown by chemical vapor deposition. Nat. Commun. *12*, 809. https://doi.org/10.1038/s41467-021-21072-z.

Mi, Y., Zhang, Z., Zhao, L., Zhang, S., Chen, J., Ji, Q., Shi, J., Zhou, X., Wang, R., Shi, J., et al. (2017). Tuning excitonic properties of monolayer MoS$_2$ with microsphere cavity by high-throughput chemical vapor deposition method. Small *13*, 1701694. https://doi.org/10.1002/smll.201701694.

Peng, B., Li, Q., Liang, X., Song, P., Li, J., He, K., Fu, D., Li, Y., Shen, C., Wang, H., et al. (2017). Valley polarization of trions and magnetoresistance in heterostructures of MoS$_2$ and yttrium iron garnet. ACS Nano *11*, 12257–12265. https://doi.org/10.1021/acsnano.7b05743.

Salehzadeh, O., Djavid, M., Tran, N.H., Shih, I., and Mi, Z. (2015). Optically pumped two-dimensional MoS$_2$ lasers Operating at room-temperature. Nano Lett. *15*, 5302–5306. https://doi.org/10.1021/acs.nanolett.5b01665.

Schwarz, S., Dufferwiel, S., Walker, P.M., Withers, F., Trichet, A.A.P., Sich, M., Li, F., Chekhovich, E.A., Borisenko, D.N., Kolesnikov, N.N., et al. (2014). Two-dimensional metal-chalcogenide films in tunable optical microcavities. Nano Lett. *14*, 7003–7008. https://doi.org/10.1021/nl503312x.

Seyler, K.L., Zhong, D., Klein, D.R., Gao, S., Zhang, X., Huang, B., Navarro-Moratalla, E., Yang, L., Cobden, D.H., McGuire, M.A., et al. (2017). Ligand-field helical luminescence in a 2D ferromagnetic insulator. Nat. Phys. *14*, 277–281. https://doi.org/10.1038/s41567-017-0006-7.

Song, T., Cai, X., Tu, M.W.-Y., Zhang, X., Huang, B., Wilson, N.P., Seyler, K.L., Zhu, L., Taniguchi, T., Watanabe, K., et al. (2018). Giant tunneling magnetoresistance in spin-filter van der Waals heterostructures. Science *360*, 1214–1218. https://doi.org/10.1126/science.aar4851.

Song, T., Fei, Z., Yankowitz, M., Lin, Z., Jiang, Q., Hwangbo, K., Zhang, Q., Sun, B., Taniguchi, T., Watanabe, K., et al. (2019). Switching 2D

magnetic states via pressure tuning of layer stacking. Nat. Mater. *18*, 1298–1302. https://doi.org/10.1038/s41563-019-0505-2.

Sun, Z., Yi, Y., Song, T., Clark, G., Huang, B., Shan, Y., Wu, S., Huang, D., Gao, C., Chen, Z., et al. (2019). Giant nonreciprocal second-harmonic generation from antiferromagnetic bilayer CrI$_3$. Nature *572*, 497–501. https://doi.org/10.1038/s41586-019-1445-3.

Verzhbitskiy, I.A., Kurebayashi, H., Cheng, H., Zhou, J., Khan, S., Feng, Y.P., and Eda, G. (2020). Controlling the magnetic anisotropy in Cr$_2$Ge$_2$Te$_6$ by electrostatic gating. Nat. Electron. *3*, 460–465. https://doi.org/10.1038/s41928-020-0427-7.

Wang, H., Liu, Y., Wu, P., Hou, W., Jiang, Y., Li, X., Pandey, C., Chen, D., Yang, Q., Wang, H., et al. (2020a). Above room-temperature ferromagnetism in wafer-scale two-dimensional van der Waals Fe$_3$GeTe$_2$ tailored by a topological insulator. ACS Nano *14*, 10045–10053. https://doi.org/10.1021/acsnano.0c03152.

Wang, X., Cao, J., Lu, Z., Cohen, A., Kitadai, H., Li, T., Tan, Q., Wilson, M., Lui, C.H., Smirnov, D., et al. (2021). Spin-induced linear polarization of photoluminescence in antiferromagnetic van der Waals crystals. Nat. Mater. https://doi.org/10.1038/s41563-021-00968-7.

Wang, Y., Deng, L., Wei, Q., Wan, Y., Liu, Z., Lu, X., Li, Y., Bi, L., Zhang, L., Lu, H., et al. (2020b). Spin-valley locking effect in defect states of monolayer MoS$_2$. Nano Lett. *20*, 2129–2136. https://doi.org/10.1021/acs.nanolett.0c00138.

Webster, L., and Yan, J.-A. (2018). Strain-tunable magnetic anisotropy in monolayer CrCl$_3$, CrBr$_3$, and CrI$_3$. Phys. Rev. B *98*. https://doi.org/10.1103/PhysRevB.98.144411.

Wu, S., Buckley, S., Jones, A.M., Ross, J.S., Ghimire, N.J., Yan, J., Mandrus, D.G., Yao, W., Hatami, F., Vučković, J., et al. (2014). Control of two-dimensional excitonic light emission via photonic crystal. 2D Mater. *1*, 011001. https://doi.org/10.1088/2053-1583/1/1/011001.

Wu, S., Buckley, S., Schaibley, J.R., Feng, L., Yan, J., Mandrus, D.G., Hatami, F., Yao, W., Vuckovic,

J., Majumdar, A., et al. (2015). Monolayer semiconductor nanocavity lasers with ultralow thresholds. Nature *520*, 69–72. https://doi.org/10.1038/nature14290.

Yang, S., Xu, X., Zhu, Y., Niu, R., Xu, C., Peng, Y., Cheng, X., Jia, X., Huang, Y., Xu, X., et al. (2021). Odd-even layer-number effect and layer-dependent magnetic phase diagrams in MnBi$_2$Te$_4$. Phys. Rev. X *11*, 011003. https://doi.org/10.1103/PhysRevX.11.011003.

Ye, Y., Wong, Z.J., Lu, X., Ni, X., Zhu, H., Chen, X., Wang, Y., and Zhang, X. (2015). Monolayer excitonic laser. Nat. Photon. *9*, 733–737. https://doi.org/10.1038/nphoton.2015.197.

Zhang, W.-B., Qu, Q., Zhu, P., and Lam, C.-H. (2015). Robust intrinsic ferromagnetism and half semiconductivity in stable two-dimensional single-layer chromium trihalides. J. Mater. Chem. C *3*, 12457–12468. https://doi.org/10.1039/c5tc02840j.

Zhang, X.-X., Li, L., Weber, D., Goldberger, J., Mak, K.F., and Shan, J. (2020). Gate-tunable spin waves in antiferromagnetic atomic bilayers. Nat. Mater. *19*, 838–842. https://doi.org/10.1038/s41563-020-0713-9.

Zhao, L., Shang, Q., Gao, Y., Shi, J., Liu, Z., Chen, J., Mi, Y., Yang, P., Zhang, Z., Du, W., et al. (2018). High-temperature continuous-wave pumped lasing from large-area monolayer semiconductors grown by chemical vapor deposition. ACS Nano *12*, 9390–9396. https://doi.org/10.1021/acsnano.8b04511.

Zheng, G., Xie, W.-Q., Albarakati, S., Algarni, M., Tan, C., Wang, Y., Peng, J., Partridge, J., Farrar, L., Yi, J., et al. (2020). Gate-tuned interlayer coupling in van der Waals ferromagnet Fe$_3$GeTe$_2$nanoflakes. Phys. Rev. Lett. *125*, 047202. https://doi.org/10.1103/PhysRevLett.125.047202.

Zhong, D., Seyler, K.L., Linpeng, X., Cheng, R., Sivadas, N., Huang, B., Schmidgall, E., Taniguchi, T., Watanabe, K., McGuire, M.A., et al. (2017). Van der Waals engineering of ferromagnetic semiconductor heterostructures for spin and valleytronics. Sci. Adv. *3*, e1603113. https://doi.org/10.1126/sciadv.1603113.

STAR★METHODS

KEY RESOURCES TABLE

REAGENT or RESOURCE	SOURCE	IDENTIFIER
Chemicals		
Chromium powder	Alfa Aesar	CAS: 7440-47-3
anhydrous iodine particles	Alfa Aesar	CAS: 7553-56-2
SiO$_2$ microsphere	Tianjin BigGoose Scientific Co., Ltd	Item: S2-13000
Software and algorithms		
Adobe Illustrator	www.adobe.com	CC 2018
Origin	www.originlab.com	2018
Other		
Optical microscopy	Motic	BA310MET
Confocal Raman Imaging	WITec	alpha300 R
Thermal evaporation system	Leybold	UNIVEX250
Scanning Electron Microscope	Thermo Fisher Scientific	JSM-7600F

RESOURCE AVAILABILITY

Lead contact

Further information and requests for resources and materials should be directed to the lead contact, Prof. Bo Peng (bo_peng@uestc.edu.cn).

Materials availability

This study did not generate new unique reagents.

Date and code availability

Data reported in this paper will be shared by the lead contact upon request. No new code was generated during this study.

EXPERIMENTAL MODEL AND SUBJECT DETAILS

Sample preparation

CrI$_3$ and MoS$_2$ flakes were mechanically exfoliated from bulk crystal onto polydimethylsiloxane films and then transferred onto SiO$_2$/Si substrates. The commercial SiO$_2$ microspheres solution were dropped onto another SiO$_2$/Si substrates, which were heated on a heating table to make the solvent completely volatilize. Next, SiO$_2$ microspheres were directly transferred onto CrI$_3$ and MoS$_2$ flakes. The samples were loaded into cold head for optical measurements in glove box.

Optical measurements

The details about the optical measurements are listed under the section "quantification and statistical analysis".

METHOD DETAILS

Materials

The SiO$_2$ microsphere solutions were ordered from Tianjin BigGoose Scientific Co., Ltd (Item: S2-13000). Chromium powder (99.99%) and iodine particles (99.99%) were supplied by Alfa Aesar. MoS$_2$ bulk crystal were bought from HQ graphene.

CrI$_3$ synthesis

About 1 g of the stoichiometric mixture of Chromium powder and iodine particles was loaded in the ampoule (16-mm inner diameter, 20-mm outer diameter, and 200-mm length), which was evacuated to a pressure of 10^{-3} Pa. The ampoule was sealed and placed into a two-zone furnace with temperature gradient of 650° to 530°C for 7 days. The CrI$_3$ crystal was obtained at the sink region of the ampoule.

Sample preparation

The details about the sample preparation are listed under the section "experimental model and subject details".

QUANTIFICATION AND STATISTICAL ANALYSIS

Scanning electron microscopy (SEM)

The morphologies of CrI$_3$ flakes and SiO$_2$ microspheres were observed with JEOL JSM-7600M field-emission scanning electron microscope.

Raman spectroscopy

The Raman spectra were recorded by Witec Alpha 300R Plus confocal Raman microscope (1800 groves/mm grating), coupled with a closed-cycle He optical cryostat (10 K) and a 7 T magnetic field. The excitation laser of 514 nm was 2.5 mW and the integration time was 60 s. The polarization-resolved Raman spectra were obtained by rotating a half-wave plate in crossed-polarization configuration.

Photoluminescence spectroscopy

The PL signal were recorded by Witec Alpha 300R Plus confocal Raman microscope (150 groves/mm grating), coupled with a closed-cycle He optical cryostat (10 K) and a 7 T magnetic field. The excitation laser of 633 nm was 2 mW and the integration time was 15 s.

Reflective magnetic circular dichroism spectroscopy

A 633 nm HeNe laser with ~2 μW was coupled to the Witec Raman system through free optical path for RMCD measurements, which was modulated by photoelastic modulator (PEM, f_{PEM} = 50 KHz) and focused onto samples by a long working distance 50✕ objective (NA = 0.45). The reflected beams were collected by the same objective, passed through a non-polarizing beamsplitter cube into an APD photodetector.